EXTENDED PDF FORMAT
SPONSORED BY
usb
www.usbweb.com

A High-Frequency Secondary Event During the 2004 Parkfield Earthquake

Bettina P. Allmann, *et al.*

Science **318**, 1279 (2007);
DOI: 10.1126/science.1146537

The following resources related to this article are available online at www.sciencemag.org (this information is current as of March 31, 2008):

Updated information and services, including high-resolution figures, can be found in the online version of this article at:
http://www.sciencemag.org/cgi/content/full/318/5854/1279

Supporting Online Material can be found at:
http://www.sciencemag.org/cgi/content/full/318/5854/1279/DC1

This article **cites 22 articles**, 11 of which can be accessed for free:
http://www.sciencemag.org/cgi/content/full/318/5854/1279#otherarticles

This article appears in the following **subject collections**:
Geochemistry, Geophysics
http://www.sciencemag.org/cgi/collection/geochem_phys

Information about obtaining **reprints** of this article or about obtaining **permission to reproduce this article** in whole or in part can be found at:
http://www.sciencemag.org/about/permissions.dtl

Science (print ISSN 0036-8075; online ISSN 1095-9203) is published weekly, except the last week in December, by the American Association for the Advancement of Science, 1200 New York Avenue NW, Washington, DC 20005. Copyright 2007 by the American Association for the Advancement of Science; all rights reserved. The title *Science* is a registered trademark of AAAS.

mote ligation in the LC phase relative to that in the isotropic. Additionally, every ligation in the LC phase produces an extended complementary oligomer. In this case, the formation of the LC phase by the complementary duplexes has the autocatalytic effect of establishing conditions that would strongly promote their own growth into longer complementary chains relative to the non–LC-forming oligomers. The fact that the liquid crystal ordering is found to depend sensitively on complementarity introduces selectivity into this process and means that the overall structure of the complementary assemblies generated will actually be templated by the liquid crystal geometry. This appears to have been the case for the linear rodlike structure of base-paired polynucleotides.

References and Notes

1. R. E. Franklin, R. G. Gosling, *Nature* **171**, 740 (1953).
2. J. E. Lydon, *Liq. Cryst. Today* **12**, 1 (2003).
3. M. H. F. Wilkins, A. R. Stokes, H. R. Wilson, *Nature* **171**, 738 (1953).
4. V. Luzzati, V. A. Nicolaieff, *J. Mol. Biol.* **1**, 127 (1959).
5. C. Robinson, *Tetrahedron* **13**, 219 (1961).
6. F. Livolant, A. M. Levelut, J. Doucet, J. P. Benoit, *Nature* **339**, 724 (1989).
7. R. L. Rill, T. E. Strzelecka, M. W. Davidson, D. H. van Winkle, *Physica A* **176**, 87 (1991).
8. K. Merchant, R. L. Rill, *Biophys. J.* **73**, 3154 (1997).
9. F. Livolant, F. A. Leforestier, *Prog. Polym. Sci.* **21**, 1115 (1996).
10. R. Podgornik, H. H. Strey, V. A. Parsegian, *Curr. Opin. Colloid Interface Sci.* **3**, 534 (1998).
11. R. Brandes, D. R. Kearns, *Biochemistry* **25**, 5890 (1986).
12. T. M. Alam, G. Drobny, *J. Chem. Phys.* **92**, 6840 (1990).
13. P. J. Hagerman, *Annu. Rev. Biophys. Biophys. Chem.* **17**, 265 (1988).
14. L. Onsager, *Ann. N.Y. Acad. Sci.* **51**, 627 (1949).
15. P. Bolhuis, D. Frenkel, *J. Chem. Phys.* **106**, 666 (1997).
16. Materials and methods are available as supporting material on *Science* Online.
17. M. P. Taylor, J. Herzfeld, *Langmuir* **6**, 911 (1990).
18. X. Lu, J. T. Kindt, *J. Chem. Phys.* **120**, 10328 (2004).
19. P. Van der Schoot, M. E. Cates, *Langmuir* **10**, 670 (1994).
20. R. Hentschke, J. Herzfeld, *Phys. Rev. A* **44**, 1148 (1991).
21. J. V. Selinger, R. F. Bruinsma, *Phys. Rev. A* **43**, 2922 (1991).
22. V. R. Horowitz, L. A. Janowitz, A. L. Modic, P. A. Heiney, P. J. Collings, *Phys. Rev. E Stat. Nonlin. Soft Matter Phys.* **72**, 041710 (2005).
23. R. Wing *et al.*, *Nature* **287**, 755 (1980).
24. M. R. Redinbo, L. Stewart, P. Kuhn, J. J. Champoux, W. G. J. Hol, *Science* **279**, 1504 (1998).
25. C. A. Davey, D. F. Sargent, K. Luger, A. W. Maeder, T. J. Richmond, *J. Mol. Biol.* **319**, 1097 (2002).
26. J. E. Lydon, *Curr. Opin. Colloid Interface Sci.* **8**, 480 (2004).
27. J. T. Davis, *Angw. Chem. Int. Ed.* **43**, 668 (2004).
28. M. A. Bates, D. Frenkel, *J. Chem. Phys.* **109**, 6193 (1998).
29. A. M. Bohle, R. Holyst, T. Vilgis, *Phys. Rev. Lett.* **76**, 1396 (1996).
30. H. Durchschlag, in *Thermodynamic Data for Biochemistry and Biotechnology*, H. J. Hinz, Ed. (Springer-Verlag, New York, 1986), chap. 3.
31. M. Mandelkern, J. G. Elias, D. Eden, D. M. Crothers, *J. Mol. Biol.* **152**, 153 (1981).
32. P. L. C. Teixeira, J. M. Tavares, M. M. Telo da Gama, *J. Phys. Condens. Matter* **12**, R411 (2000).
33. B. Tinland, A. Pluen, J. Strum, G. Weill, *Macromolecules* **30**, 5763 (1997).
34. S. Asakura, F. Oosawa, *J. Chem. Phys.* **22**, 1255 (1954).
35. P. J. Flory, *Macromolecules* **11**, 1138 (1978).
36. J. P. Ferris, G. Ertem, *Science* **257**, 1387 (1992).
37. T.B., N.A.C., and M.N. conceived and initiated the study. M.N. and G.Z. designed and directed the experiments. M.N. fabricated the gradient cells and performed optical studies on them. G.Z. performed the interferometry to determine DNA concentration. G.Z. fabricated and performed optical studies on the complementary/noncomplementary mixture cells. M.N., G.Z., R.P., B.C., C.J., and J.C. performed the x-ray experiments. This work was supported by a Ministero dell’ Università e della Ricerca grant COFIN-2004024508 (T.B. and G.Z), NSF grant DMR 0606528 (N.A.C. and M.N.), NSF Materials Research Science and Engineering Centers grant DMR 0213819 (N.A.C.), and DOE Nanoscale Science, Engineering, and Technology Grant 04SCPE389 (R.P. and B.D.C.). Use of the Advanced Photon Source was supported by the U.S. Department of Energy under contract DE-AC02-06CH11357.

Supporting Online Material

www.sciencemag.org/cgi/content/full/318/5854/1276/DC1
Materials and Methods
Figs. S1 to S5
References and Notes

16 April 2007; accepted 3 October 2007
10.1126/science.1143826

A High-Frequency Secondary Event During the 2004 Parkfield Earthquake

Bettina P. Allmann* and Peter M. Shearer

By using seismic records of the 2004 magnitude 6.0 Parkfield earthquake, we identified a burst of high-frequency seismic radiation that occurred about 13 kilometers northwest of the hypocenter and 5 seconds after rupture initiation. We imaged this event in three dimensions by using a waveform back-projection method, as well as by timing distinct arrivals visible on many of the seismograms. The high-frequency event is located near the south edge of a large slip patch seen in most seismic and geodetic inversions, indicating that slip may have grown abruptly at this point. The time history obtained from full-waveform back projection suggests a rupture velocity of 2.5 kilometers per second. Energy estimates for the subevent, together with long-period slip inversions, indicate a lower average stress drop for the northern part of the Parkfield earthquake compared with that for the region near its hypocenter, which is in agreement with stress-drop estimates obtained from small-magnitude aftershocks.

The 2004 magnitude (*M*) 6.0 Parkfield earthquake on the San Andreas Fault (SAF) in central California was well recorded by a dense network of seismic and geodetic sensors installed in anticipation of this event. The wealth of available data permits studying the rupture process of a moderate-sized crustal earthquake in detail. Results to date show that the earthquake ruptured about 20 km northward from the hypocenter over about 10 s. However, ground accelerations near the fault exhibit large variations, and the high-frequency (HF) waves radiated by the earthquake are not yet fully understood. We show that a large burst of HF energy occurred about 5 s into the earthquake, as seen both in full-waveform back projection of strong motion data and in the timing of a clear secondary arrival that is observed on many of the records.

We used acceleration data from the General Earth Observing System (GEOS) array, the California Geological Survey (CGS) array, and the U.S. Geological Survey (USGS) Parkfield dense seismograph array (UPSAR). These overlapping arrays were installed in the Parkfield region over the past 2 decades in order to record an expected *M* 6.0 earthquake (*1*). The CGS array consists mostly of analog stations that are triggered on the shear wave (*S*) arrival. These data are available in digital form with a 200-Hz sample rate (*2*). Altogether, there are 73 strong motion records from these networks in a 20-km radius around the Parkfield rupture area.

These data have been used to characterize strong ground motions from the mainshock and to invert for time-dependent slip models. These inversions are generally performed at relatively long periods because of the difficulty in fitting the more variable and incoherent HF part of the records. A different approach for imaging the earthquake rupture is by means of a back projection of the seismic waveforms into the volume surrounding the rupture (*3*). This method was first applied to rupture imaging of the 2004 Sumatra-Andaman earthquake with the use of teleseismic *P* records (*4*). For Parkfield, we stacked *S* waves on the north component from 68 out of 73 local strong-motion records along the travel-time operator obtained by ray tracing from each image point to each receiver through a reference one-dimensional (1D) velocity model. We forced the onset of waveforms to focus at the known hypocenter location of the mainshock by applying a static correction for each *S* arrival before stacking. This corrects for time shifts

---

Cecil H. and Ida M. Green Institute of Geophysics and Planetary Physics, Scripps Institution of Oceanography, University of California San Diego, 9500 Gilman Drive, La Jolla, CA 92093–0225, USA.

*To whom correspondence should be addressed. E-mail: ballmann@ucsd.edu

caused by 3D velocity structure along the ray paths. Assuming that the static shifts are time-invariant and dominated by near-surface velocity variations (*3*), the backstacked energy at times later than the onset of the *S* wave train will stack coherently and image the rupture process in space and time. Before back projection, we integrated the records to velocity, bandpass filtered the data between 2 to 8 Hz, and applied an automatic gain control (AGC) over a 10-s window in order to equalize the amplitudes of the records (*3*). We tapered the influence of stations near the perimeter of the aperture with a distance-dependent weight to reduce migration artifacts (*3*). The impulse response of our source-receiver geometry and the effect of artifacts are shown in more detail in the Supporting Online Material (SOM) text and in figs. S1 to S3.

A secondary event occurring 5 s after rupture initiation is the clearest signal seen in our back-projection results (Fig. 1) and is robust with respect to changes in the stacking method. Aside from the enforced maximum at the hypocenter (Fig. 1A), we observed a secondary maximum between 6- and 8-km depth at a distance of 12 to 14 km northwest of the hypocenter (Fig. 1B). Within the resolution constraints discussed in the SOM text, we observed the maximum focus of the subevent slightly to the southwest of the SAF, which is consistent with the fault geometry deduced from the aftershock distribution (*5*). Note that the amplitude of the peaks in these images is not necessarily proportional to the radiated energy of the events because of the AGC filtering as well as defocusing effects for the secondary event caused by uncertainties in the velocity model. Investigation of the time history (SOM text and fig. S4) suggests that any rupture in the area between the hypocenter and the subevent radiated much less seismic energy in the investigated frequency band. However, our results cannot resolve whether small amounts of HF radiation were emitted continuously as the rupture propagated from the hypocenter to this northern high-energy point or whether the rupture was discontinuous and the subevent was triggered by seismic waves from the hypocenter.

The secondary event can also be detected as a distinct HF arrival in the *S*-wave coda in records from many, but not all, stations in the area. The event is visible (Fig. 2) not only as an *S*-wave arrival on local strong-motion stations but also as a *P*-wave arrival on some stations of the Southern California Seismic Network (SCSN) at regional distances greater than 100 km (Fig. 2 inset). Notably, we observe that the event is best seen on stations to the south and east of the rupture zone. Moreover, compared with the *S* arrival from the hypocenter, the delay time of the secondary event is largest for stations south of the mainshock

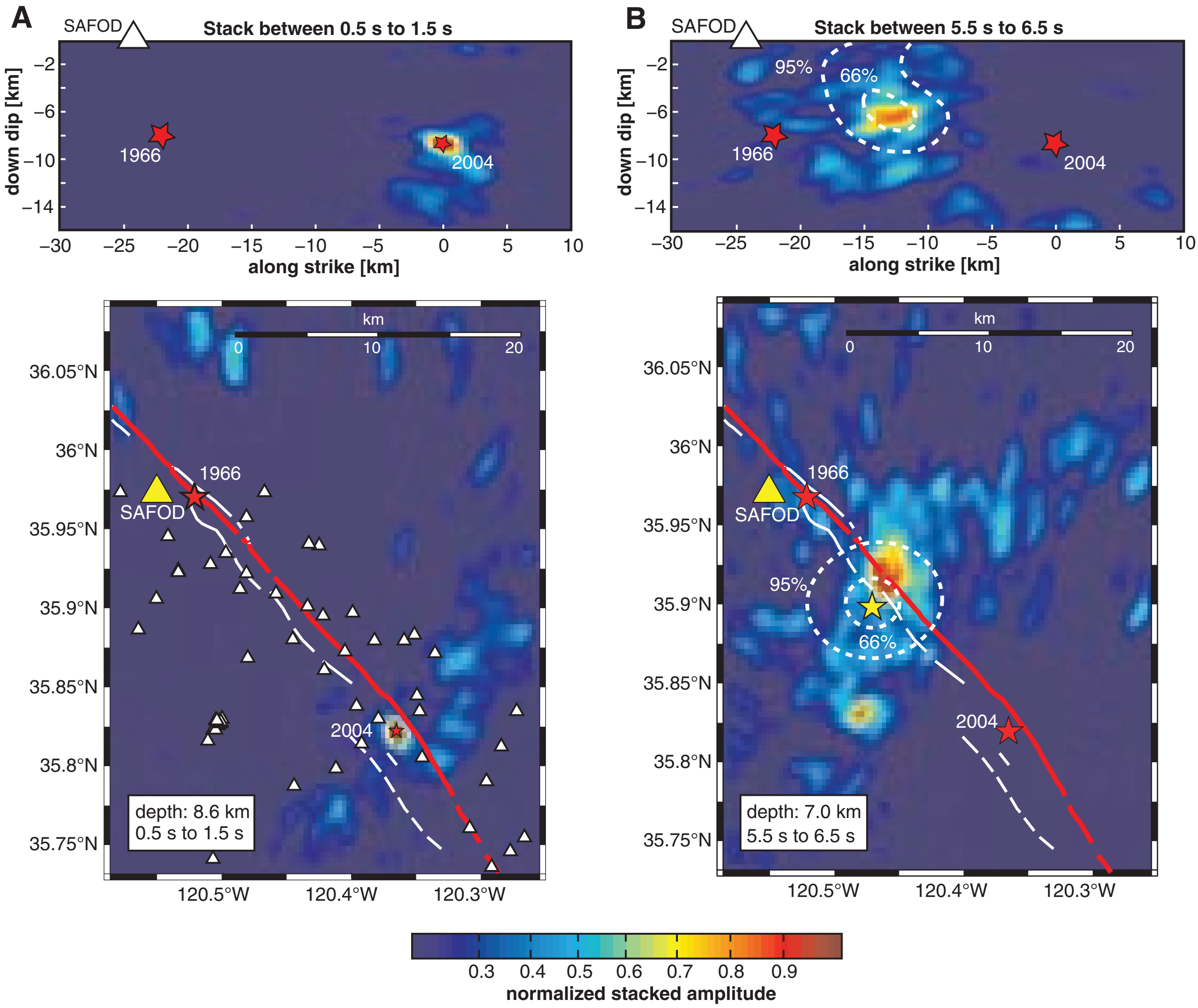

Fig. 1. Stack of backprojected amplitude for two 1-s time slices in comparison to the 66% and 95% confidence intervals (dashed) of the subevent location from travel time inversion (yellow star) for a cross section along the fault (top) and a mapview at the depth of the respective maximum (bottom). Red stars denote the hypocenters of the 1966 and the 2004 *M* 6 Parkfield earthquakes. Triangles denote strong-motion stations and the location of the San Andreas Fault Observatory at Depth (SAFOD). The surface trace of the SAF is shown as a red line. (**A**) Stack between 0.5 s to 1.5 s, where we obtain a focus at the hypocenter. (**B**) Stack between 5.5 s to 6.5 s, where we obtain a focus at the subevent. The normalized amplitude is increased by a factor of 1.6 for (B).

epicenter (Fig. 3). At local stations, the event is only visible in the *S* wave train on the horizontal components, whereas it is visible in the *P* wave train at regional distances, following the P_n phase from the hypocenter at an approximately constant delay time (Fig. 3, bottom).

We picked the differential arrival times between the mainshock and subevent *S* arrivals for 15 local stations, as well as between the mainshock and subevent P_n arrival for five regional stations that clearly show secondary arrivals. In order to locate the subevent, we performed a grid-search inversion of the differential travel times for the origin time and location of the secondary phase with respect to the known location and origin time of the hypocenter (*3*). We observed a best-fitting location for the nucleation zone of the subevent about 12.5 km along the fault plane to the northwest of the hypocenter at a depth of about 6.1 km (Fig. 4A). The subevent location is offset to the southwest of the fault, although the 95% confidence interval includes the main fault trace (Fig. 1B). The inverted origin time of this subevent is 4.95 s (± 0.1 s SD) with respect to the mainshock rupture initiation. The best-fitting subevent location resulting from this inversion agrees well with the back-projection image (Fig. 1B). To check our result, we forward-calculated travel times for the best-fitting subevent location (Fig. 3) and observed a generally good fit to the picks.

From our results, we can make a number of inferences about the secondary event. First, we can reject the possibility of this event being a reflected phase from the free surface or from the Mohorovičić discontinuity (Moho) because, in this case, the inversion result would have located the event in a mirror point either above the free surface or below the Moho. Second, it is reasonable to assume that the subevent is part of, or has been triggered by, the mainshock because dividing its distance from the mainshock hypocenter by the inverted origin time difference gives a reasonable value of 2.5 km/s as an estimate of the average rupture velocity. Third, due to the northward-propagating rupture of the mainshock, the travel times for stations to the north of the subevent are very close to the arrival times of the hypocenter. This explains why the subevent is not distinguishable on stations to the north: For these stations, the subevent is buried in the coda of the initial hypocenter pulse. However, it is not clear why the subevent is seen more distinctly on stations east of the fault compared with those to the west. Because of the lack of clear observations of the secondary arrival at stations to the north, the P_n observations to the south are critical for obtaining a reliable location for the subevent. With local *S* arrival times alone, there is a severe tradeoff between the event origin time and its location along the fault. In contrast to the travel time inversion, the back-projection method is able to clearly resolve the location of the secondary event with only *S* waveforms from local stations and does not require observations at regional distances. The close agreement seen in the location of the subevent between the two methods (Fig. 1) provides a good check on the internal consistency of the observations.

Sources of HF arrivals during the Parkfield *M* 6.0 rupture have also been identified by applying an array beam-forming technique on records of the small-aperture UPSAR (*6*). The northernmost inferred source (Fig. 4C), with the largest correlation and the largest acceleration pulse at the UPSAR array, likely is associated with our HF subevent (SOM text). The inferred average rupture velocity of about 2.4 km/s for this source is in good agreement with our observation of about 2.5 km/s.

Previous analyses of HF radiation from large earthquakes were often based on inversion of envelopes (*7*–*9*) and found sources of HF radiation located near the boundary of high slip zones. These inversions were limited to equal or lower resolution than slip inversions of low-frequency waveforms. Observations of HF radiation of great subduction earthquakes found

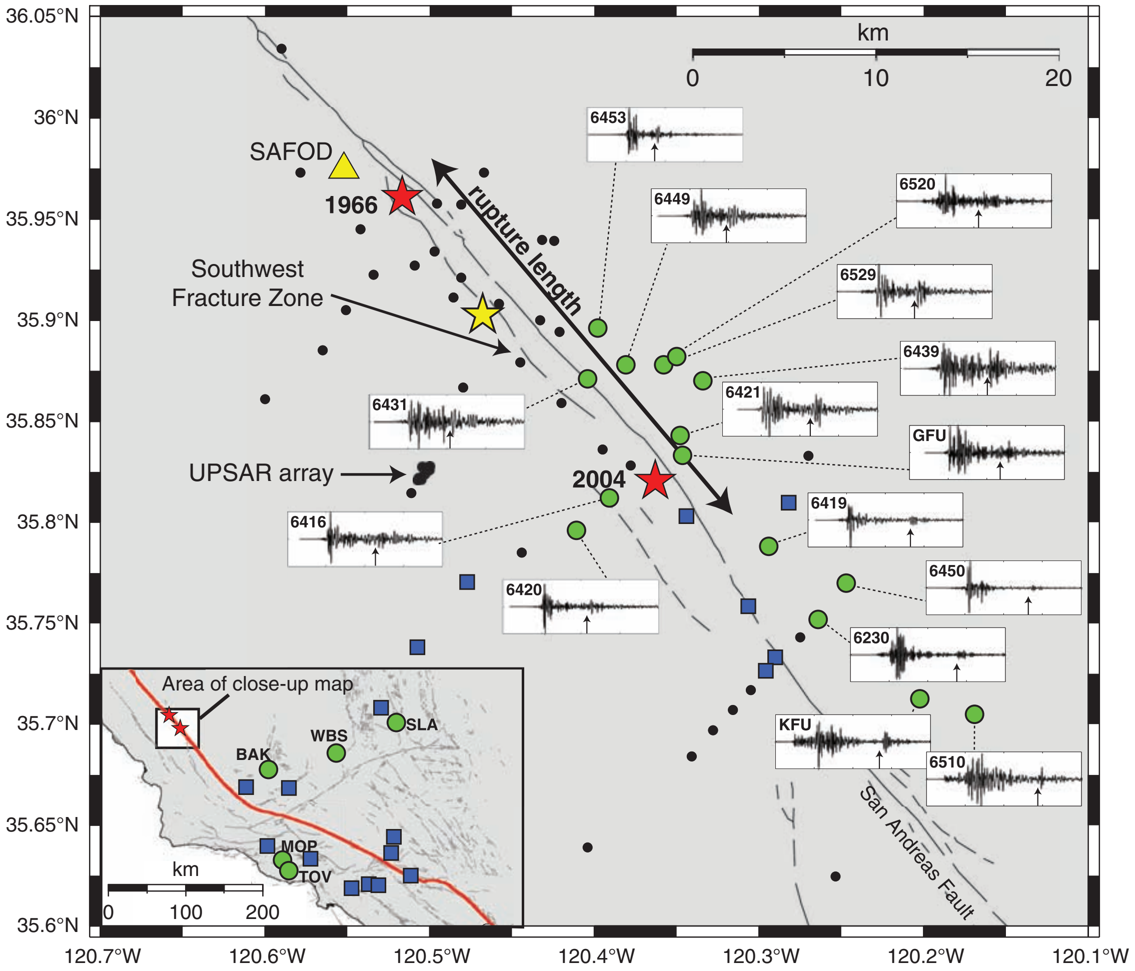

Fig. 2. Strong-motion stations in the Parkfield area and in southern California used in the investigation. Green dots denote stations where the secondary phase can be seen clearly (arrows in seismograms). Blue squares denote stations where the event is less prominent. Small black dots denote local stations where the event could not be visually detected. The displayed seismograms show 20 s of N-component acceleration data starting 5 s before the *S* first arrival, bandpass-filtered between 2 and 8 Hz. Red stars mark the epicenters of the 2004 and the 1966 *M* 6.0 Parkfield earthquakes, whereas the yellow star denotes the subevent location. The SAF surface trace and subsidiary faults are indicated by black lines.

sources of HF radiation near the end of the rupture but could not resolve whether the HF source was associated with the boundary of a slip patch or possibly with a stopping phase (*10*, *11*). Previous studies all have in common that a specific fault plane geometry, on which slip or HF radiation is to be inverted, is assumed a priori. The study presented here differs in two aspects: (i) We obtained increased resolution by direct back propagation of waveforms, thus omitting the step of forward-calculating and inverting individual waveforms, and (ii) we performed the back propagation in 3D, which allows a volumetric mapping of seismic radiation sources and does not require an assumption about any particular fault plane.

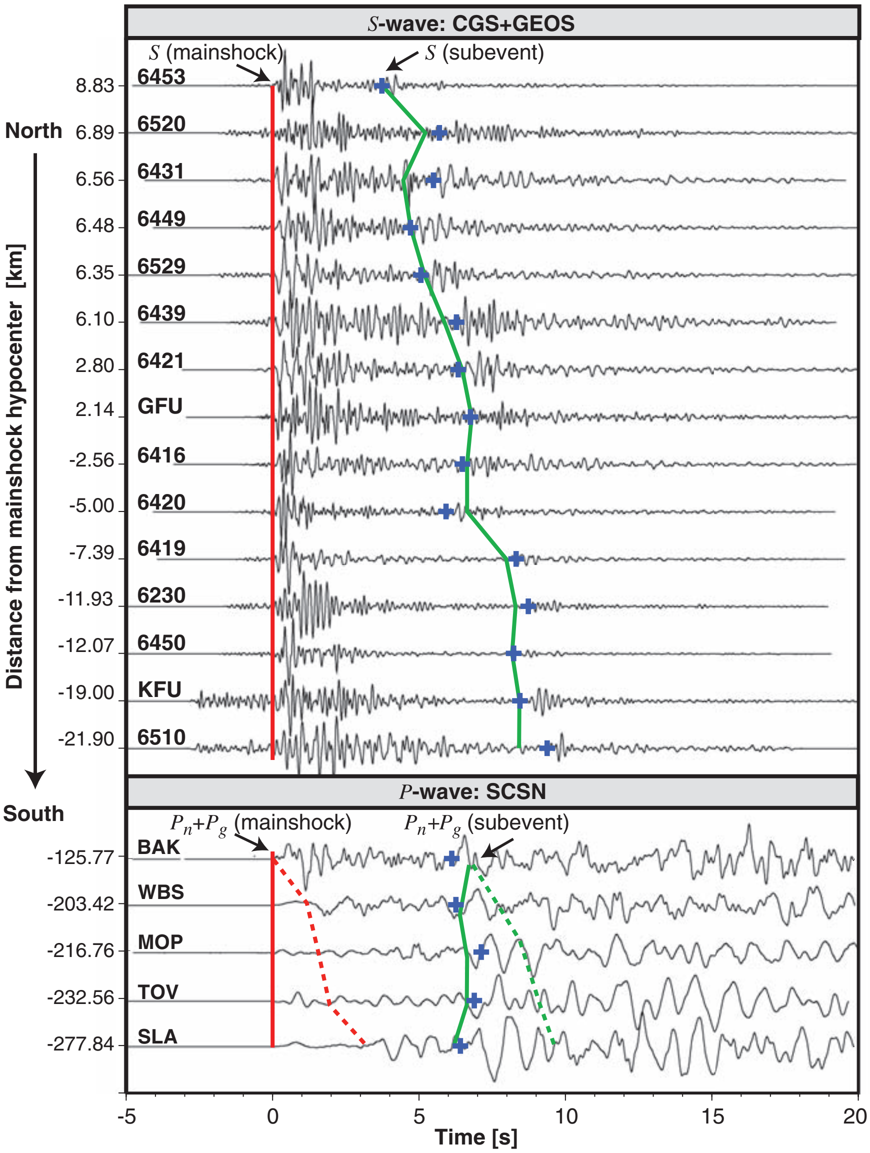

Fig. 3. Record section of the 2004 Parkfield mainshock for 15 local CGS and GEOS stations (**top**) and 5 regional SCSN stations (**bottom**) that clearly show secondary arrivals. The local data were bandpass-filtered between 2 and 8 Hz. The local stations are aligned along the *S*-wave arrival, and the regional stations are aligned along the P_n arrival from the hypocenter (red solid). The blue crosses denote the picked secondary phase arrivals for *S* and P_n. The solid green curve shows the theoretical arrival of the inverted best-fitting subevent location. Red and green dotted lines mark the theoretical P_g arrival of the hypocenter and the subevent, respectively. All stations are sorted with respect to distance from the hypocenter from north to south.

An important aspect of our result is the location of our subevent with respect to slip patches found in rupture models from long-period data. Compared to the slip model of (*12*), which had been derived from a subset of the strong motion data used in our study at lower frequencies between 0.16 and 1 Hz (Fig. 4B), our subevent is located at the southern edge of the northern high-slip patch. This observation is similar for a number of other slip models inverted by using various data and methods (*1*, *13*, *14*, *15*). Although these differ considerably in the details, they all have in common a broad region of high slip about 10 to 20 km north of the hypocenter (Fig. 4C). However, there are some fundamental differences between the data and methods used to locate the subevent and those used to invert for the slip models. Geodetic constraints on slip are based on the permanent coseismic displacement across the fault and say nothing about the dynamics of the rupture. Slip inversions from strong-motion data such as (*12*) (Fig. 4B) are typically based on filtered low-frequency waveforms below 1 Hz. On the other hand, we find the clearest observations of the subevent at frequencies higher than 1 to 2 Hz (fig. S5). Theoretical results show that enhanced HF radiation likely emanates from areas of changes in slip and/or rupture velocity or direction (*16*) and is therefore expected to occur at the edges of the slip areas inverted from low frequencies (*17*). Numerical simulations based on published slip models (*18*) or using complex fault geometries (*19*) indicate that HF energy radiation is concentrated near the initiation point of asperities or near changes in fault geometry. Comparison of our result with the slip model of (*12*) (Fig. 4B) reveals that our HF subevent is located in an area of high slip gradient, which is consistent with the numerical results and suggests that the rupture may have broken an asperity at this point, thus initiating the large moment release to the north seen in the long-period inversions. Geodetic slip models (Fig. 4C) are of lower resolution and may not be compared at this level of detail, even though we observed a consistent pattern among them. Both (*12*) and (*6*) report evidence for an increase in rupture velocity toward the north. We cannot resolve any changes in rupture velocity between the two events from the time history (fig. S4), mainly because we do not observe continuous HF radiation. The distribution of seismicity in the rupture area remains stationary before and after the 2004 *M* 6.0 Parkfield earthquake (*20*), with the bulk of the microseismicity distributed along a "streak" between 4- and 6-km depth, and a "hole" below (*21*) (Fig. 4A). We note that the slip area found by (*12*) largely coincides with the seismicity hole, except for an area between 5 and 12 km north of the hypocenter where little slip is observed. Our subevent is located within the seismicity hole, at the transition between this area of small slip and a large patch of high slip to the northwest, pointing to a change in slip amplitude as the main cause for the HF event.

By estimating the average slip area and slip amplitude from the various slip models for the two slip patches near the hypocenter and to the north of the subevent, we can obtain an estimate of the seismic moment, M_0, associated with these slip patches. The models indicate that the bulk of the moment release occurred on the northern slip patch with a seismic moment about 2 to 20 times higher than the slip area near the hypocenter, with values of 6×10^{17} to 9×10^{17} Nm, which correspond to a magnitude of $M_w = 5.8$ to 5.9 for the northern subevent.

In comparison, assuming that the radiated seismic energy, E_R, is proportional to our observed amplitudes (SOM text), we observe that the northern slip patch radiates one to five times less energy than the mainshock. From E_R and M_0 we can calculate the scaled energy (*22*), $\tilde{e} = E_R/M_0$, which is proportional to stress drop for a number of standard earthquake rupture models. The fact that the secondary event had a higher moment release than the initial event while radiating comparable or lesser amounts of seismic energy suggests that the northern slip event had a smaller average stress drop than that of the southern event. Our stress-drop results are consistent with the location of the subevent in a low stress-drop region computed from the background seismicity (*23*). On the other hand, the region around the mainshock hypocenter is dominated by relatively high stress-drop events in the background seismicity. These patterns of high and low stress-drop results were observed to be largely unchanged by the occurrence of the 2004 mainshock (*23*). These results suggest that at least some of the dynamic properties of large earthquake ruptures may be predictable from observations of small earthquakes near the fault. Strong heterogeneities in observed stress drops along a fault or changes in fault geometry may be an indication to expect heterogeneous slip behavior and associated HF radiation from a major or characteristic earthquake along the same fault segment.

These results indicate that waveform back projection can resolve changes in the rupture dynamics of crustal earthquakes in the M 6 range by imaging the source of HF seismic radiation. If adequate station coverage is available, this method is suited to be applied in an automated way to obtain near-real-time images of the rupture. Such images may help in the discrimination of the actual fault plane and may thus be useful for hazard assessment and guidance for emergency services.

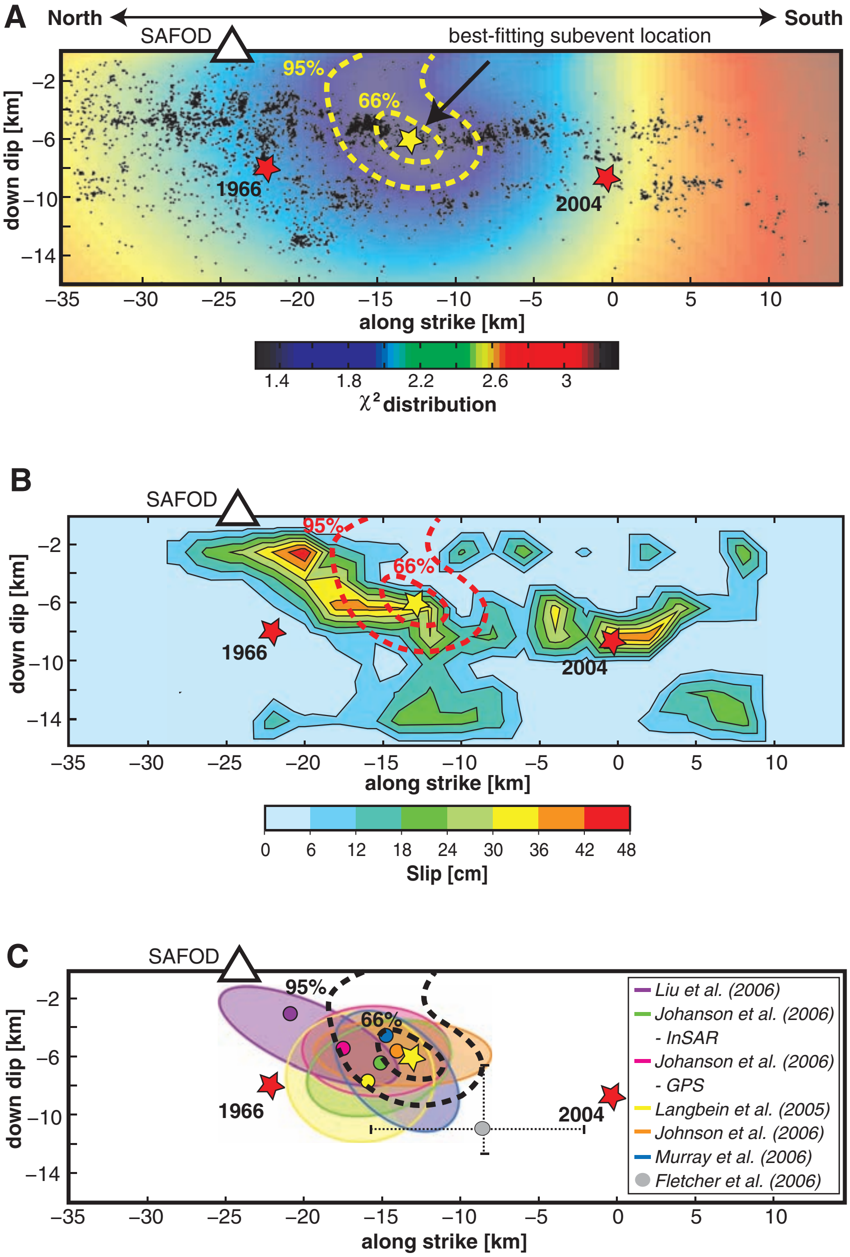

Fig. 4. Inversion result for locating the secondary event. The best-fitting location is shown as the yellow star including the 95% and 66% confidence intervals (dashed). The 1966 and 2004 hypocenters are shown as red stars. (**A**) The colors mark the logarithmic values of the χ^2 distribution. About 6000 relocated aftershocks of the 2004 mainshock are shown as black dots. (**B**) Comparison between the subevent location (yellow star) and the strong-motion slip inversion model obtained from (*12*). (**C**) Comparison between the subevent location and high-slip areas at the northern part of the mainshock rupture zone from various slip models (colored ellipses). The colored dots mark the observed maximum slip for the respective models. The location of a HF source during the mainshock rupture obtained from beamforming analysis at UPSAR (*6*) is also included as a gray dot, together with the location error bars (dotted lines).

References and Notes

1. J. Langbein *et al.*, *Seismol. Res. Lett.* **76**, 10 (2005).
2. A. F. Shakal, H. Haddadi, V. Graizer, K. Lin, M. Huang, *Bull. Seismol. Soc. Am.* **96**, S90 (2006).
3. Methods are available on *Science* Online.
4. M. Ishii, P. M. Shearer, H. Houston, J. E. Vidale, *Nature* **435**, 933 (2005).
5. R. W. Simpson, M. Barall, J. Langbein, J. R. Murray, M. J. Rymer, *Bull. Seismol. Soc. Am.* **96**, S28 (2006).
6. J. Fletcher, P. Spudich, L. Baker, *Bull. Seismol. Soc. Am.* **96**, S129 (2006).
7. Y. Zeng, K. Aki, T. Teng, *J. Geophys. Res.* **98**, 11981 (1993).
8. Y. Kakehi, K. Irikura, *Geophys. J. Int.* **125**, 892 (1996).
9. H. Nakahara, T. Nishimura, H. Sato, M. Ohtake, *J. Geophys. Res.* **103**, 855 (1998).
10. T. Sato, K. Imanishi, M. Kosuga, *Geophys. Res. Lett.* **23**, 33 (1996).
11. W. Nakayama, M. Takeo, *Bull. Seismol. Soc. Am.* **87**, 918 (1997).
12. P. Liu, S. Custódio, R. Archuleta, *Bull. Seismol. Soc. Am.* **96**, S143 (2006).
13. I. Johanson, E. Fielding, F. Rolandone, R. Bürgmann, *Bull. Seismol. Soc. Am.* **96**, S269 (2006).
14. K. Johnson, R. Bürgmann, K. Larson, *Bull. Seismol. Soc. Am.* **96**, S321 (2006).
15. J. Murray, J. Langbein, *Bull. Seismol. Soc. Am.* **96**, S283 (2006).
16. R. Madariaga, *Geophys. J. R. Astron. Soc.* **51**, 625 (1977).
17. P. Spudich, L. Frazer, *Bull. Seismol. Soc. Am.* **74**, 2061 (1984).
18. S. Ide, *Bull. Seismol. Soc. Am.* **92**, 2994 (2002).
19. R. Madariaga, J. Ampuero, M. Adda-Bedia, *Geophys. Monogr. Am. Geophys. Union* **170**, 223 (2006).
20. C. Thurber *et al.*, *Bull. Seismol. Soc. Am.* **96**, S38 (2006).
21. F. Waldhauser, W. Ellsworth, D. Schaff, A. Cole, *Geophys. Res. Lett.* **31**, L18608 (2004).
22. H. Kanamori, L. Rivera, *Geophys. Monogr. Ser.* **170**, 3 (2006).
23. B. Allmann, P. Shearer, *J. Geophys. Res.* **112**, B04305 (2007).
24. We are grateful to A. Goertz for valuable comments and suggestions. This research was funded by National Earthquake Hazards Reduction Program/USGS grant 03HQPA0001 and supported by the Southern California Earthquake Center (SCEC). SCEC is funded by NSF cooperative agreement EAR-0106924 and USGS cooperative agreement 02HQAG0008. The SCEC contribution number for this paper is 1121.

Supporting Online Material

www.sciencemag.org/cgi/content/full/318/5854/1279/DC1
Materials and Methods
SOM Text
Figs. S1 to S5

15 June 2007; accepted 15 October 2007
10.1126/science.1146537